

# Multiwavelength monitoring and X-ray brightening of Be X-ray binary PSR J2032+4127/MT91 213 on its approach to periastron

Wynn C. G. Ho<sup>1,2\*</sup>, C.-Y. Ng<sup>3</sup>, Andrew G. Lyne<sup>4</sup>, Ben W. Stappers<sup>4</sup>, Malcolm J. Coe<sup>2</sup>, Jules P. Halpern<sup>5</sup>, Tyrel J. Johnson<sup>6†</sup>, Iain A. Steele<sup>7</sup>

<sup>1</sup>Mathematical Sciences and STAG Research Centre, University of Southampton, Southampton, SO17 1BJ, UK

<sup>2</sup>Physics and Astronomy and STAG Research Centre, University of Southampton, Southampton, SO17 1BJ, UK

<sup>3</sup>Department of Physics, the University of Hong Kong, Hong Kong, China

<sup>4</sup>Jodrell Bank Centre for Astrophysics, School of Physics and Astronomy, University of Manchester, Manchester, M13 9PL, UK

<sup>5</sup>Columbia Astrophysics Laboratory, Columbia University, New York, NY, 10027, USA

<sup>6</sup>College of Science, George Mason University, Fairfax, VA, 22030, USA

<sup>7</sup>Astrophysics Research Institute, Liverpool John Moores University, Liverpool, L3 5RF, UK

Accepted 2016 September 19. Received 2016 September 14; in original form 2016 August 19

## ABSTRACT

The radio and gamma-ray pulsar PSR J2032+4127 was recently found to be in a decades-long orbit with the Be star MT91 213, with the pulsar moving rapidly towards periastron. This binary shares many similar characteristics with the previously unique binary system PSR B1259–63/LS 2883. Here, we describe radio, X-ray, and optical monitoring of PSR J2032+4127/MT91 213. Our extended orbital phase coverage in radio, supplemented with *Fermi* LAT gamma-ray data, allows us to update and refine the orbital period to 45–50 yr and time of periastron passage to 2017 November. We analyse archival and recent *Chandra* and *Swift* observations and show that PSR J2032+4127/MT91 213 is now brighter in X-rays by a factor of  $\sim 70$  since 2002 and  $\sim 20$  since 2010. While the pulsar is still far from periastron, this increase in X-rays is possibly due to collisions between pulsar and Be star winds. Optical observations of the H $\alpha$  emission line of the Be star suggest that the size of its circumstellar disc may be varying by  $\sim 2$  over timescales as short as 1–2 months. Multiwavelength monitoring of PSR J2032+4127/MT91 213 will continue through periastron passage, and the system should present an interesting test case and comparison to PSR B1259–63/LS 2883.

**Key words:** stars: emission line, Be – stars: individual: MT91 213 – stars: neutron – pulsars: individual: PSR B1259–63, PSR J2032+4127 – X-rays: binaries – X-rays: individual: PSR B1259–63, PSR J2032+4127.

## 1 INTRODUCTION

Recent radio observations of the 143 ms pulsar PSR J2032+4127 find it to be part of a very eccentric, long orbital period binary system, with the pulsar expected to reach periastron in late 2017 with its high-mass, Be star companion (Lyne et al. 2015). The pulsar was discovered by *Fermi* LAT (Abdo et al. 2009) and is associated with TeV source TeV J2032+4130 (Camilo et al. 2009). These characteristics make the PSR J2032+4127 binary system very similar to the previously unique pulsar system PSR B1259–63/LS 2883 (see, e.g. Dubus 2013, for review), and X-ray results reported here support this similarity.

Subsequent to its discovery in gamma rays, PSR J2032+4127 was detected in radio by Camilo et al. (2009), who also reanal-

ysed a 49 ks *Chandra* observation taken in 2004 of the field of the Cygnus OB2 association (at a distance  $d = 1.33 \pm 0.06$  kpc; Kiminki et al. 2015), to which the pulsar likely belongs. They confirm an X-ray source at the position of the radio source, which also corresponds to optical source 213 of Massey & Thompson (1991), a B0 V star (hereafter MT91 213). MT91 213 has a mass of either  $14.5 M_{\odot}$  (Wright et al. 2015) or  $17.5 M_{\odot}$  (Kiminki et al. 2007) and bolometric luminosity  $L_{\text{bol}} = 1.51 \times 10^4 L_{\odot} = 5.79 \times 10^{37}$  erg s<sup>-1</sup> (Wright et al. 2015), in broad agreement with values appropriate to its spectral and luminosity classification, i.e.  $15.0 \pm 2.8 M_{\odot}$  and  $16100 \pm 130 L_{\odot}$  (Hohle et al. 2010). An optical spectrum shows MT91 213 has a H $\alpha$  equivalent width (EW) of  $-12.6 \text{ \AA}$  (Camilo et al. 2009), which is typical of Be stars and due to a circumstellar disc surrounding the star. Camilo et al. (2009) fit a power-law to the *Chandra* spectrum and find an unabsorbed 0.5–10 keV X-ray luminosity  $L_X \approx 6 \times 10^{30}$  erg s<sup>-1</sup> ( $d/1.3 \text{ kpc}$ )<sup>2</sup>. This X-ray luminosity is compatible with that of either Be stars (see, e.g. Berghöfer et al. 1997; Gagné et al. 2011; Nazé et al. 2014) or pul-

\* Email: wynnho@slac.stanford.edu

† Present address: Naval Research Laboratory, Washington, DC, 20375, USA

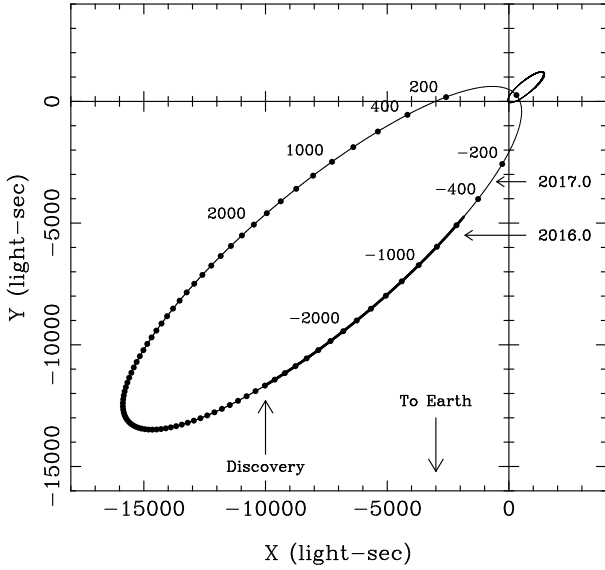


**Figure 1.** Schematic diagram illustrating the approximate orbital motion of PSR J2032+4127 and its Be-star companion MT91 213 about their common centre of mass. The orbit shown is that of model 2 (see Table 1), which has an orbital period  $P_b = 17000$  d and is projected on to the plane containing the line of sight and major axis of the orbit. The inclination  $i$  of the plane of the orbit to the plane of the sky is assumed to be  $60^\circ$ . The circles mark 200 d intervals and indicate time from predicted epoch of periastron, MJD 58069. The pulsar moves counter-clockwise in the diagram and has been approaching the Be star since discovery in late 2008/early 2009. The thick line shows the portion of the pulsar orbit covered by radio observations reported here, MJD 54689–57538. Note that orbital velocity is proportional to the separation between the circles, with a 1000-light-second separation indicating a velocity of about  $18 \text{ km s}^{-1}$ . The small ellipse near the origin shows the orbit of the Be star, assuming that it has a mass of  $15 M_\odot$  and that the pulsar has a mass of  $1.35 M_\odot$ .

sars of age  $\sim 10^5$  yr (see, e.g. Yakovlev & Pethick 2004; Page et al. 2006; Potekhin et al. 2015), where the pulsar age is taken to be its characteristic spin-down age.

More recent analysis of timing observations of PSR J2032+4127 reveals that its timing noise can be removed by considering a timing model in which the pulsar is in an eccentric (with eccentricity  $e > 0.94$ ), decades-long orbit (Lyne et al. 2015). Because of the long orbital period, radio measurements up to that time only cover about 20% of the orbit, and previous observations (at all wavelengths) of the pulsar/Be-star binary system have been when the pulsar is on the apastron-side of the orbit. Fig. 1 shows a schematic diagram of the system. Radio and gamma-ray telescopes continue to monitor the pulsar as it moves towards periastron. These observations will refine the orbital parameters, including eccentricity and mass function, and could, along with VLBI measurements, directly determine distance and orbital inclination (Lyne et al. 2015).

Many of the above characteristics are typical of Be X-ray binary systems, albeit with orbital periods of  $\lesssim 1$  yr, which can shine at up to Eddington luminosities ( $10^{38} \text{ erg s}^{-1}$ ) when the neutron star nears periastron and accretes matter from the circumstellar disc (of size a few times the Be star radius, and larger for isolated Be stars; Klus et al. 2014; Reig et al. 2016) of its Be star companion (Reig 2011). In this work, we are concerned with X-ray (as well as radio and optical) emission when the pulsar is far from periastron and not accreting from the circumstellar disc of the Be star, which

might occur near periastron. Thus the X-ray luminosity is expected to be much lower, as indeed we find, as well as a brightening that seems in accord with the well-studied 3.4 yr orbital period gamma-ray binary that contains PSR B1259–63. There are several previous *Chandra* observations of Cygnus OB2 (see Table 2), and although significantly off-axis, some of these contain the pulsar/Be-star binary system in the field of view. As discussed above, Camilo et al. (2009) describe results for the 2004 observation (ObsID 4501), while Rauw et al. (2015) describe results for the 2010 observations (ObsID 10944, 10945, 10951, 10962).

In Section 2, we report results of an updated timing solution based on monitoring at radio wavelengths, supplemented with *Fermi* LAT gamma-ray data. We (re)analyse all *Chandra* and *Swift* X-ray data, as well as our 2016 4.9 ks *Chandra* Target of Opportunity observation, and report our results in Section 3. In Section 4, we report on recent optical measurements of the  $H\alpha$  EW and their implication for the size of the Be star circumstellar disc. In Section 5, we summarize and briefly discuss our findings, including a few comparisons with PSR B1259–63/LS 2883.

## 2 RADIO AND GAMMA-RAY OBSERVATIONS AND REVISED TIMING SOLUTION

Because of limited orbital phase coverage of observations of the pulsar since its discovery in 2009, there was strong covariance between several parameters of the orbital configuration reported in Lyne et al. (2015). Radio timing observations with the 76-m Lovell Telescope at Jodrell Bank continued during the subsequent two years. These observations, along with gamma-ray times of arrival (TOAs; see next), are all processed using the methodology described in Lyne et al. (2015), which uses the TEMPO2 (Hobbs et al. 2006) pulsar timing analysis package. Timing data now span a total of nearly 8 years, i.e. Modified Julian Date (MJD) 54689–57538.

Data from *Fermi* LAT are used to provide gamma-ray profiles and additional TOAs over the timespan of the radio data. We select Pass 8 LAT data, belonging to the SOURCE class as defined under the P8R2\_SOURCE\_V6 instrument response functions, from the start of the mission (2008 August 4) to 2016 May 23 (MJD 54682–57527) in a circular region of interest (ROI) centred on the pulsar position and with a  $15^\circ$  radius. We choose events with energies from 100 MeV to 100 GeV and require the zenith angle to be  $\leq 90^\circ$ . We restrict time intervals to be when LAT was in nominal science operations, data are flagged as good, and there are no corresponding bright solar flares or gamma-ray bursts. We perform a binned maximum likelihood analysis on a  $20^\circ \times 20^\circ$  square region, including all sources in the 3FGL catalogue within  $25^\circ$  of the ROI centre (Acero et al. 2015). Diffuse emission components are modelled using *gll\_iem\_v06.fits* (Acero et al. 2016) and *iso\_P8R2\_SOURCE\_V6\_v06.txt* templates<sup>1</sup>. Analysis of spatial and spectral residuals does not reveal the need for any additional components.

Following the procedure outlined in Abdo et al. (2013), we model the gamma-ray spectrum of PSR J2032+4127 as either a power law, power law with exponential cutoff, or power law with exponential cutoff and free exponential index  $b$ . We compare the best-fitting likelihood using each model and find significant curvature ( $\sim 25\sigma$ ) and a preference for the model with  $b$

<sup>1</sup> <http://fermi.gsfc.nasa.gov/ssc/data/access/lat/BackgroundModels.html>

being free ( $\sim 3\sigma$ ). The best-fitting model has a power law photon index of  $1.47 \pm 0.03$ , cutoff energy of  $4.49 \pm 0.37$  GeV, and  $b = 0.89 \pm 0.04$ ; uncertainties are purely statistical errors. These values do not agree, within uncertainties, with those of [Abdo et al. \(2013\)](#), but we note that their analysis uses three years of P7\_V6 data and finds  $TS_{b,\text{free}} = 0$  and thus uses  $b \equiv 1$ . We perform spectral fits in  $\sim 30$  day bins of 95 flux measurements with only the normalization of PSR J2032+4127 free and calculate a value of  $TS_{\text{var}}$  (as defined in [Acero et al. 2015](#)) of 109, which is less than the threshold value of 128.80 and indicates no detectable flux variability [with a 1–100 GeV flux of  $(2.42 \pm 0.04) \times 10^{-8}$  photon  $\text{cm}^{-2} \text{s}^{-1}$ , consistent with that of [Acero et al. 2015](#)]. Using the best-fit model with  $b$  being free and events within  $3^\circ$  of the ROI centre, we calculate spectral weights to enhance sensitivity ([Kerr 2011](#)). We then use the weighted events to construct 95 TOAs (at  $\sim 30$ -day cadence) as described in [Ray et al. \(2011\)](#).

The newly extended orbital phase coverage reduces covariance between fitted parameters and allows refinement of the timing model. While we cannot yet obtain a unique solution because the orbital period and eccentricity are still highly covariant, there is a one-dimensional family of TEMPO2 fits, which are summarized in Fig. 2, as a function of orbital period. The rms timing residuals reach an asymptotic minimum at about 0.42 ms for orbital periods approaching 17830 d, the period at which eccentricity is close to 1.0 and the system would be marginally bound. However, the mass function  $f_m [= (M_{\text{OB}} \sin i)^3 / (M_{\text{OB}} + M_{\text{NS}})^2$ , where  $M_{\text{NS}}$  and  $M_{\text{OB}}$  are the neutron star and Be star masses and  $i$  is the orbital inclination] has a maximum value of  $\approx 15 M_\odot$  [using  $M_{\text{NS}} = 1.35 M_\odot$ ,  $M_{\text{OB}} = 17.5 M_\odot$  (see Sec. 1), and  $i = 90^\circ$ ], and Fig. 2 shows that  $f_m = 15 M_\odot$  corresponds to a binary period of 17670 d. Inspection of timing residuals from the best-fitting long-period models indicates that timing residuals are essentially ‘white’, with little evidence of any systematic departure of TOAs from the models. For periods shorter than about 16000 d, substantial systematic departures are seen, resulting in an observed increase in rms residuals. Any solution with orbital period of  $16000 < P_b < 17670$  days, with corresponding eccentricity of  $0.94 < \epsilon < 0.99$ , is likely to be acceptable. Parameters of three models spanning this acceptable range are presented in Table 1. For all such acceptable fits, the epoch of periastron is becoming well constrained at around MJD 58060(10), i.e. centred on early November 2017. Figure 1 illustrates one possible configuration of the system for  $P_b = 17000$  d and  $\epsilon = 0.96$  (model 2 in Table 1). We note that there is no systematic deviation between radio and gamma-ray residuals through the whole data set, indicating that the ephemeris and dispersion measure (DM) are correct and that there is no detectable variation in DM yet.

In summary, we conclude that PSR J2032+4127 is in a very eccentric and weakly bound system with an orbital period of  $\approx 45$ –50 years. We now expect periastron to occur around the beginning of November 2017. However, we caution that the pulsar is rather young, with a characteristic age of about 200 kyr, and it may therefore suffer from some rotational timing noise. Our conclusions are based on the assumption that the pulsar is a perfect rotator and is not subject to significant timing noise which would distort measured Keplerian parameters of the binary system. On the other hand, the best models show little evidence for any unmodelled timing noise. Furthermore, as the pulsar approaches periastron, rapidly-changing Doppler effects are likely to dominate any effects of timing noise.

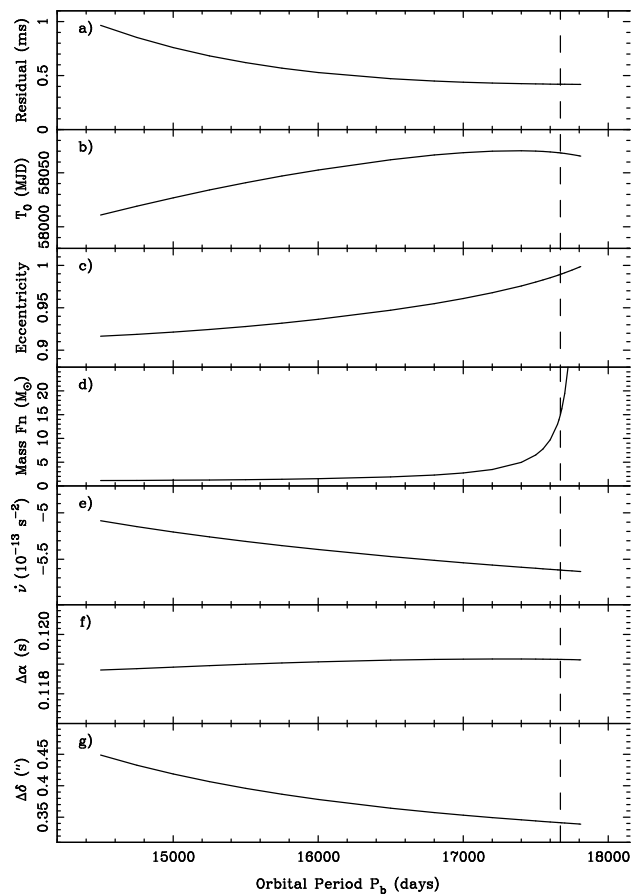


**Figure 2.** Results of fits to TOAs of a number of binary models having different fixed values of orbital period  $P_b$ : (a) rms timing residual  $\sigma_t$ , (b) epoch of periastron  $T_0$ , (c) orbital eccentricity  $\epsilon$ , (d) mass function  $f_m$ , (e) pulsar rotational frequency derivative  $\dot{\nu}$ , (f) deviation of right ascension of pulsar  $\Delta\alpha$  from  $20^{\text{h}}32^{\text{m}}13^{\text{s}}$ , (g) deviation of declination  $\Delta\delta$  from  $41^\circ27'24''$ . Solutions to the right of the vertical dashed line (at  $P_b = 17670$  d) are disallowed by the pulsar and Be star masses ( $f_m \leq 15 M_\odot$ ; see text). Parameters for  $P_b = 16000$  (Model 1),  $17000$  (Model 2), and  $17670$  d (Model 3) are given in Table 1.

### 3 X-RAY OBSERVATIONS AND RESULTS

#### 3.1 *Chandra*

The field of PSR J2032+4127/MT91 213 is covered by several archival *Chandra* observations made with the ACIS-I detector. We also obtained a targeted 4.9 ks exposure using ACIS-S on 2016 Feb 24. Details of these observations are given in Table 2.

We carry out all *Chandra* data reduction and analysis using CIAO 4.8 with CALDB 4.7.1. We reprocess the data using the script `chandra_repro`, which applies the latest calibration. A subset of images in the energy range 0.5–7 keV is shown in Fig. 3. There are four other sources within  $\sim 20''$  of PSR J2032+4127, and their count-rates are listed in Table 3 (from the 2010 observations, only ObsID 10951 is used since these sources are located far off-axis in other exposures). Cygnus OB2 4 is a O7 III(f) star ([Walborn 1973](#)). MT91 216 and MT91 221 are stars 216 and 221, respectively, of [Massey & Thompson \(1991\)](#), with MT91 216 being a B1.5 V star and MT91 221 being a B2 V star ([Kiminki et al. 2007](#)). From optical spectra, [Camilo et al. \(2009\)](#)

**Table 1.** Binary model fits to TOAs of PSR J2032+4127. Fitted values of parameters are given for three representative models that span the best-fitting range of orbital periods, i.e. 16000 d (Model 1), 17000 d (Model 2), and 17670 d (Model 3). Models with periods shorter than that of model 1 have unacceptably large timing residuals, while those with periods longer than that of model 3 are disallowed by the pulsar and Be star masses (see text).  $1\sigma$  uncertainties in the last digit(s) are given in parentheses. Data used in our analysis spans the range MJD 54689–57538. The units of time are Barycentric Dynamical Time.

Parameter	Model 1	Model 2	Model 3
Right ascension, $\alpha$ (J2000.0)	20 <sup>h</sup> 32 <sup>m</sup> 13. <sup>s</sup> 119(2)	20 <sup>h</sup> 32 <sup>m</sup> 13. <sup>s</sup> 119(2)	20 <sup>h</sup> 32 <sup>m</sup> 13. <sup>s</sup> 119(2)
Declination, $\delta$ (J2000.0)	41°27′24″38(2)	41°27′24″35(2)	41°27′24″34(2)
Epoch of frequency, $t_0$ (MJD)	55700.0	55700.0	55700.0
Frequency, $\nu_0$ (Hz)	6.980979(5)	6.980975(6)	6.980973(7)
Frequency time derivative, $\dot{\nu}_0$ ( $10^{-12}\text{s}^{-2}$ )	-0.5396(5)	-0.5538(4)	-0.5617(5)
Orbital period, $P_b$ (d)	16000	17000	17670
Epoch of periastron, $T_0$ (MJD)	58053(1)	58069(1)	58068(2)
Projected semi-major axis, $x$ (light-second)	7138(48)	9022(216)	16335(3737)
Eccentricity, $\epsilon$	0.936(1)	0.961(2)	0.989(5)
Longitude of periastron, $\omega$ (deg)	52(1)	40(1)	21(5)
Mass function, $f_m$ ( $M_\odot$ )	1.5	2.7	15.0
Glitch epoch, $T_g$ (MJD)	55810.77	55810.77	55810.77
Frequency, $\Delta\nu_g$ ( $10^{-6}$ Hz)	1.9064(1)	1.9073(1)	1.9076(1)
Frequency time derivative, $\Delta\dot{\nu}_g$ ( $10^{-15}\text{s}^{-2}$ )	-0.501(8)	-0.545(7)	-0.564(6)
DM ( $\text{pc cm}^{-3}$ )	114.68(3)	114.67(2)	114.66(2)
DM time derivative, DM1 ( $\text{pc cm}^{-3}\text{yr}^{-1}$ )	-0.02(1)	-0.01(1)	-0.01(1)
rms timing residual, $\sigma_t$ (ms)	0.53	0.44	0.42

**Table 2.** *Chandra* and *Swift* observations of PSR J2032+4127/MT91 213. *Chandra* and *Swift* count-rates are computed for 0.3–7 keV and 0.3–10 keV, respectively. Unabsorbed 0.3–10 keV flux  $F_{0.3-10}^{\text{unabs}}$  is calculated from count-rate using WebPIMMS and assuming  $N_{\text{H}} = 7.7 \times 10^{21} \text{ cm}^{-2}$  and a power law  $\Gamma = 2$ . Errors are  $1\sigma$ .

Telescope	ObsID	Date	MJD	Exposure ks	Count-rate ks <sup>-1</sup>	$F_{0.3-10}^{\text{unabs}}$ $10^{-13} \text{ erg cm}^{-2} \text{ s}^{-1}$
<i>Chandra</i>	4358	2002 Aug 11	52497.83	4.9	0.8 ± 0.4	0.2 ± 0.1
<i>Chandra</i>	4501	2004 Jul 19	53205.09	48.7	1.6 ± 0.2	0.51 ± 0.06
<i>Swift</i>	37744001	2008 Jun 16	54633.04	10.8	1.0 ± 0.4	1.0 ± 0.4
<i>Chandra</i>	10944	2010 Feb 1	55228.46	28.3	3.6 ± 0.3	1.1 ± 0.1
<i>Chandra</i>	10945	2010 Feb 1	55228.80	27.9	2.3 ± 0.2	0.72 ± 0.08
<i>Chandra</i>	10951	2010 Feb 11	55238.58	29.2	2.6 ± 0.3	0.83 ± 0.09
<i>Chandra</i>	10962	2010 Feb 22	55249.66	29.4	1.9 ± 0.2	0.60 ± 0.08
<i>Swift</i>	32767001	2013 Mar 28	56379.88	2.7	0.5 ± 0.4	0.5 ± 0.5
<i>Swift</i>	32767002	2013 Mar 29	56380.17	3.9	2.0 ± 1.0	2.0 ± 1.0
<i>Swift</i>	32767003	2015 Sep 19	57284.13	9.2	4.6 ± 0.7	4.6 ± 0.7
<i>Swift</i>	34282001	2016 Jan 22	57409.71	7.6	4.8 ± 0.8	4.9 ± 0.9
<i>Chandra</i>	18788	2016 Feb 24	57442.35	4.9	25.9 ± 2.3	6.6 ± 0.6
<i>Swift</i>	34282002	2016 Mar 4	57451.00	5.9	6.2 ± 1.0	6.3 ± 1.1
<i>Swift</i>	34282003	2016 Mar 18	57465.38	3.4	5.2 ± 1.3	5.3 ± 1.3
<i>Swift</i>	34282004	2016 Apr 1	57479.04	3.4	3.8 ± 1.1	3.8 ± 1.1
<i>Swift</i>	34282005	2016 Apr 15	57493.69	3.7	6.2 ± 1.3	6.3 ± 1.3
<i>Swift</i>	34282006	2016 May 1	57509.82	3.5	6.6 ± 1.4	6.7 ± 1.4
<i>Swift</i>	34282007	2016 May 4	57512.03	2.5	8.7 ± 1.9	8.9 ± 2.0
<i>Swift</i>	34282008	2016 May 16	57524.20	3.3	8.3 ± 1.6	8.4 ± 1.6
<i>Swift</i>	34282009	2016 May 27	57535.33	3.3	3.2 ± 1.0	3.2 ± 1.1
<i>Swift</i>	34282010	2016 Jun 1	57540.02	2.1	11.2 ± 2.3	11.4 ± 2.4
<i>Swift</i>	34282011	2016 Jun 11	57550.17	0.80	5.9 ± 2.8	6.0 ± 2.8
<i>Swift</i>	34282012	2016 Jun 18	57557.54	0.92	3.8 ± 2.1	3.9 ± 2.2
<i>Swift</i>	34282014	2016 Jul 4	57573.83	3.1	14.0 ± 2.2	14.3 ± 2.2
<i>Swift</i>	34282016	2016 Jul 10	57579.16	1.8	7.8 ± 2.1	7.9 ± 2.2
<i>Swift</i>	34282017/8	2016 Jul 22	57591.45	6.9	12.7 ± 1.4	12.9 ± 1.4
<i>Swift</i>	34282023	2016 Aug 19	57619.25	5.0	6.6 ± 1.2	6.7 ± 1.2
<i>Swift</i>	34282024	2016 Sep 2	57633.16	3.4	11.4 ± 1.9	11.6 ± 1.9

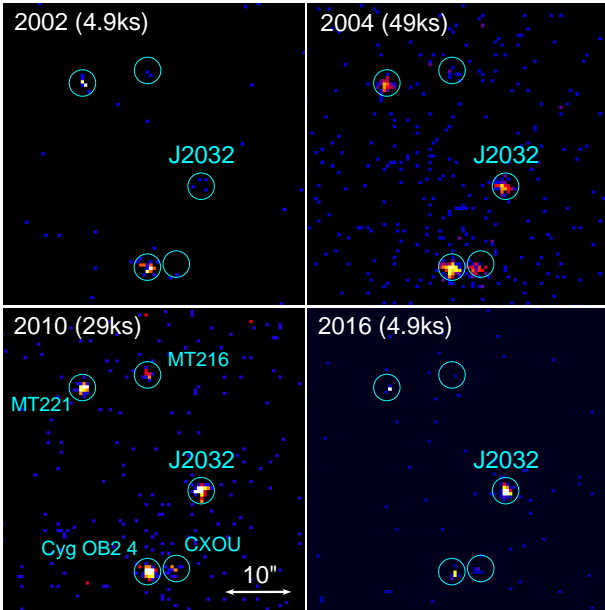


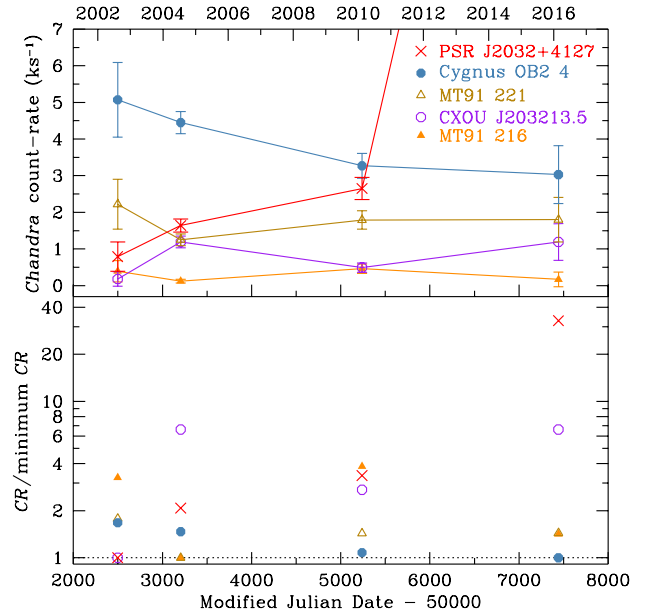
**Figure 3.** *Chandra* field of PSR J2032+4127/MT91 213 in 2002, 2004, 2010, and 2016, with PSR J2032+4127 and four nearby sources (CXOU J203213.5+412711, Cygnus OB2 4, MT91 216, and MT91 221) indicated by circles and labelled. North is up, and east is left.

identify CXOU J203213.5+412711 as a Be star that is also in Cygnus OB2.

Accounting for the different exposure times of each image shown in Fig. 3, it is clear that PSR J2032+4127 is significantly brighter at the present time than in previous epochs and relative to neighboring X-ray sources. This is demonstrated quantitatively in Fig. 4, which shows count-rates as a function of time. The top panel shows *Chandra* 0.3–7 keV background-subtracted count-rates, while the bottom panel shows relative count-rates and highlights the maximum change in brightness of each source. PSR J2032+4127 shows a monotonic increase in brightness, and its variability is significantly larger (relative increase by a factor of 33) compared to nearby X-ray sources. Cygnus OB2 4 and MT91 221, the two brightest sources other than PSR J2032+4127, vary by  $\lesssim 2$ . While the two faint sources CXOU J203213.5+412711 and MT91 216 seem to vary by  $\lesssim 7$ , this variability is possibly due to low counts and contamination by Cygnus OB2 4 in the case of CXOU J203213.5+412711. Our findings for Cygnus OB2 4, MT91 221, and CXOU J203213.5+412711 are consistent with those of Murakami et al. (2011), who examined variability between the 2002 and 2004 data.

To perform spectral analyses, we extract the source spectrum from circular apertures of radius ranging from  $2''.5$  for on-axis observations to  $9''.5$  for far off-axis ones. The background spectrum is obtained from nearby source-free regions. We did not extract a spectrum from the 2002 observation, since only four photons are detected at the pulsar position. We assume that the spectrum did not change during the four 2010 observations and combine these four to improve the signal-to-noise ratio. Spectral fits are performed using the *Sherpa* package in the 0.5–7 keV energy range. Spectra are binned such that there are at least ten counts per bin, and the statistic from Gehrels (1986) is used.

We fit either a power law model or an optically thin thermal plasma (APEC) model (see Section 5) and accounted for the

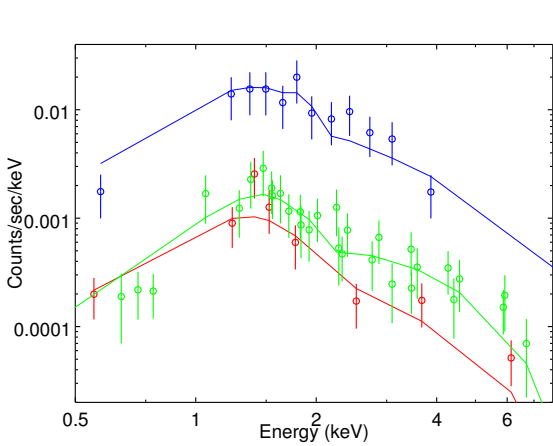


**Figure 4.** *Chandra* light curve of PSR J2032+4127/MT91 213 and nearby X-ray sources (see Fig. 3). Top panel: Points (and  $1\sigma$  error bars) are 0.3–7 keV background-subtracted count-rate (see Table 3). Note that the 2016 point for PSR J2032+4127 is at a count-rate of  $26 \text{ ks}^{-1}$ . Bottom panel: Points are count-rate (CR) from the top panel relative to minimum count-rate of each source, i.e. count-rate in 2002 for PSR J2032+4127, 2016 for Cygnus OB2 4, 2004 for MT91 221, 2002 for CXOU J203213.5+412711, and 2004 for MT91 216.

interstellar absorption using the model *tbabs* with Wilms et al. (2000) abundances. We first fit all the spectra independently. We then fit all the spectra with a single absorption column density  $N_{\text{H}}$ . Next we assume  $N_{\text{H}} = 7.7 \times 10^{21} \text{ cm}^{-2}$  (based on the color excess of MT91 213; Camilo et al. 2009) and fit each spectrum independently and jointly (see Fig. 5 for results using the power law model). Parameters between different epochs are formally consistent, although fit parameters are not well constrained. Therefore we also fit spectra jointly with the same parameters but allow different normalization between observations. All results are listed in Table 4, with  $1\sigma$  errors. Our results using a power law or APEC model for the 2004 data are consistent with those in Camilo et al. (2009), who find  $\Gamma = 2.1 \pm 0.7$ ,  $kT = 4_{-2}^{+9} \text{ keV}$ , and  $F_{0.5-10}^{\text{unabs}} = 0.32 \times 10^{-13} \text{ erg cm}^{-2} \text{ s}^{-1}$ . For the 2010 data, our results with the APEC model are comparable to those in Rauw et al. (2015), who find  $N_{\text{H}} = 7.9 \times 10^{21} \text{ cm}^{-2}$ ,  $kT = 4_{-1}^{+2} \text{ keV}$ , normalization =  $2.4 \times 10^{-5}$ , and  $F^{\text{abs}} = 0.26 \times 10^{-13} \text{ erg cm}^{-2} \text{ s}^{-1}$ . Incidentally, a thermal plasma model fit to the spectra of PSR B1259–63 near apastron gives  $kT \approx 6 - 14 \text{ keV}$  (Hirayama et al. 1999). Finally we fit all observations with the same normalization, but this yielded poor results ( $\chi^2_{\nu} > 2$ ). It is important to note that while the models we use generally yield good fits and parameters that are consistent within the large errors, the spectra are of relatively low quality, given the low number of counts ( $< 130$  counts in each observation) in the early epochs when PSR J2032+4127 is dim and the short exposure when PSR J2032+4127 is bright.

**Table 3.** *Chandra* observations of sources near PSR J2032+4127/MT91 213. Count-rates are computed for 0.3–7 keV. Errors are  $1\sigma$ .

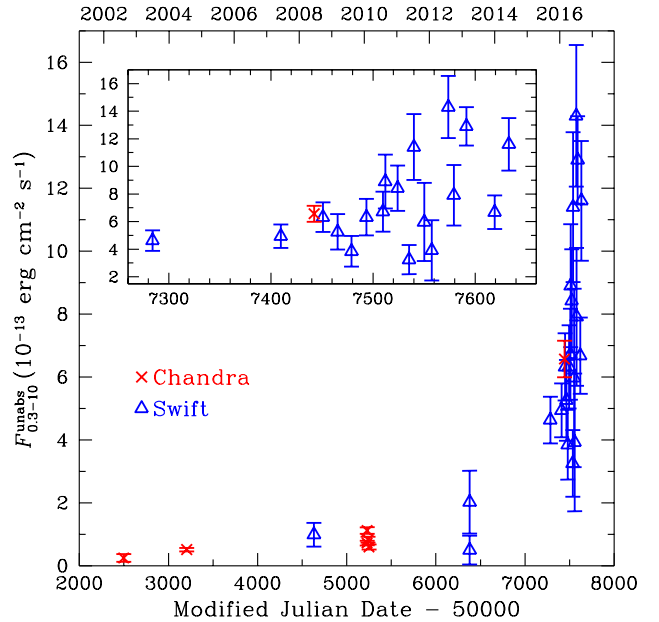
Date	Count-rate ( $\text{ks}^{-1}$ )				
	PSR J2032+4127/MT91 213	Cygnus OB2 4	MT91 221	CXOU J203213.5+412711	MT91 216
2002 Aug 11	$0.8 \pm 0.4$	$5.1 \pm 1.0$	$2.2 \pm 0.7$	$0.2 \pm 0.2$	$0.4 \pm 0.3$
2004 Jul 19	$1.6 \pm 0.2$	$4.4 \pm 0.3$	$1.2 \pm 0.2$	$1.2 \pm 0.2$	$0.1 \pm 0.1$
2010 Feb 11	$2.6 \pm 0.3$	$3.3 \pm 0.3$	$1.8 \pm 0.2$	$0.5 \pm 0.1$	$0.5 \pm 0.1$
2016 Feb 24	$25.9 \pm 2.3$	$3.0 \pm 0.8$	$1.8 \pm 0.6$	$1.2 \pm 0.5$	$0.2 \pm 0.2$

**Figure 5.** *Chandra* ACIS-I spectrum of PSR J2032+4127/MT91 213 in 2004 (red) and 2010 (green) and ACIS-S spectrum in 2016 (blue). Lines are best-fit spectra using an independent power law model for each observed spectrum and  $N_H$  frozen at  $7.7 \times 10^{21} \text{ cm}^{-2}$  (see Table 4).

### 3.2 *Swift*

To improve our understanding of the X-ray light curve of PSR J2032+4127, we checked archival data taken by *Swift* (Burrows et al. 2005) and obtained regular *Swift* monitoring. PSR J2032+4127 is serendipitously and intentionally inside the *Swift* field of view in many observations to date (see Table 2). These observations have exposure times ranging from 1 ks to 11 ks, and the source is detected in them. In each case, the 0.3–10 keV count-rate is determined using aperture photometry. A source region of radius 8 pixels centred on the position of PSR J2032+4127 is used and compared to a nearby background region of radius 63 pixels. Derived count-rates are listed in Table 2.

We use WebPIMMS to calculate the unabsorbed 0.3–10 keV flux for each *Chandra* and *Swift* count-rate, assuming  $N_H = 7.7 \times 10^{21} \text{ cm}^{-2}$  and  $\Gamma = 2$  power law (see Table 4), since the total number of counts in each observation is usually  $< 40$ . The resulting values are listed in Table 2 and shown in Fig. 6, and we see that the current X-ray flux is a factor of  $\sim 14/0.2 = 70$  times higher than in 2002 and  $\sim 14/0.8 \approx 20$  times higher than in 2010. Because of the spatial resolution of *Swift*, there are contributions to the *Swift* X-ray flux from the nearby sources shown in Fig. 3. However this contamination is only significant in the 2008 and possibly 2013 data. As we see from Fig. 4, the brightest sources in the field other than PSR J2032+4127 prior to 2015–2016 are Cygnus OB2 4 and MT91 221, and these likely contribute to at most  $\sim 9/(9 + 26) = 25\%$  of the *Swift* flux in the current epoch when PSR J2032+4127 has clearly brightened. We also checked

**Figure 6.** X-ray light curve of PSR J2032+4127/MT91 213 from 2002 to 2016. Points (and  $1\sigma$  error bars) are *Chandra* (crosses) and *Swift* (triangles) unabsorbed 0.3–10 keV flux (see Table 2). Inset: Closer view of the data covering the period from 2015 September to 2016 September.

that the recent flux decrease from mid to late May 2016 is not reflected in a bright nearby source during the same period.

### 4 $H\alpha$ EQUIVALENT WIDTH AND DISC SIZE

Optical spectra of MT91 213 were obtained on the MDM Observatory’s 2.4 m and 1.3 m telescopes, as well as the Liverpool 2 m telescope, with increased monitoring cadence in 2016. Figure 7 and Table 5 show the  $H\alpha$  emission line and EW measurements. The 2009 spectrum was published in Camilo et al. (2009). Here, we re-measured EW from all spectra, including the broad wings that become most apparent in 2016. Evidently the circumstellar disc was largest in 2009, as indicated by the stronger, single-peaked emission line. The double-peaked structure of more recent, weaker line profiles indicates a smaller disc, with peak separation corresponding to  $2v \sin i \approx 360 \text{ km s}^{-1}$ , where  $v$  is velocity and  $i$  is inclination angle. The He I  $\lambda 5876$  is also double peaked in these spectra.

MT91 213 does not always have detectable emission lines. They were not reported in Massey & Thompson (1991), although that study did not cover the  $H\alpha$  region. Spectra at additional epochs were reported by Salas et al. (2013) under a different name (Cygnus OB2-4 B) for the star: In 2012 September it showed no emission

**Table 4.** Spectral fit results of *Chandra* data of PSR J2032+4127/MT91 213. Absorption column density  $N_{\text{H}}$  is in units of  $10^{21} \text{ cm}^{-2}$ ,  $kT$  is in units of keV, normalization is in units of  $10^{-5}$ , and absorbed 0.5–7 keV flux  $F_{0.5-7}^{\text{abs}}$  is in units of  $10^{-13} \text{ erg cm}^{-2} \text{ s}^{-1}$ . Errors are  $1\sigma$ , and some upper/lower confidence limits are not constrained. \* indicates that the value of  $N_{\text{H}}$  is frozen.

Year	$N_{\text{H}}$	$\Gamma/kT$	Normalization	$F_{0.5-7}^{\text{abs}}$	$\chi^2/\text{dof}$
all parameters free and independent fit of all observations					
power law					
2004	$1^{+17}$	$1.8^{+2.0}_{-0.6}$	$0.4^{+2}_{-0.1}$	$0.2^{+0.1}_{-0.1}$	3.6/3
2010	$1^{+7}$	$1.5^{+0.5}_{-0.2}$	$0.7^{+0.6}_{-0.2}$	$0.4^{+0.1}_{-0.2}$	10.7/24
2016	$17^{+15}_{-12}$	$2.7^{+1.0}_{-0.9}$	$30^{+7}_{-20}$	$3^{+9}_{-3}$	4.0/8
APEC					
2004	$10^{+10}$	$1.5^{+0.6}_{-0.6}$	$2^{+2}_{-1}$	$0.1^{+0.07}_{-0.07}$	4.6/3
2010	$0^{+6}$	$16^{+12}_{-12}$	$2.9^{+1.0}_{-0.4}$	$0.4^{+0.03}_{-0.15}$	10.9/24
2016	$14^{+10}_{-9}$	$2.1^{+2.3}_{-0.7}$	$50^{+30}_{-20}$	$2^{+1}_{-1}$	3.5/8
$N_{\text{H}}$ tied and joint fit of observations					
power law					
2004	$4^{+6}$	$2.1^{+0.9}_{-0.8}$	$0.6^{+0.7}_{-0.3}$	$0.2^{+1}_{-0.2}$	20.0/37
2010	—	$1.7^{+0.5}_{-0.4}$	$1.0^{+0.7}_{-0.4}$	$0.4^{+0.6}_{-0.3}$	—
2016	—	$1.8^{+0.6}_{-0.5}$	$8^{+7}_{-4}$	$3^{+6}_{-3}$	—
APEC					
2004	$3^{+6}$	$4_{-3}$	$1.4^{+0.7}_{-0.4}$	$0.16^{+0.06}_{-0.07}$	20.3/37
2010	—	$8^{+76}_{-4}$	$3.0^{+1.0}_{-0.5}$	$0.4^{+0.1}_{-0.1}$	—
2016	—	$5^{+32}_{-3}$	$24^{+11}_{-5}$	$3^{+2}_{-2}$	—
$N_{\text{H}}$ frozen and independent fit of all observations					
power law					
2004	$7.7^*$	$2.5^{+0.7}_{-0.6}$	$0.9^{+0.4}_{-0.3}$	$0.14^{+0.1}_{-0.07}$	3.8/4
2010	—	$1.9^{+0.3}_{-0.2}$	$1.3^{+0.3}_{-0.3}$	$0.4^{+0.3}_{-0.2}$	11.8/25
2016	—	$2.1^{+0.3}_{-0.3}$	$11^{+3}_{-3}$	$3^{+1}_{-1}$	4.7/9
APEC					
2004	$7.7^*$	$2.1^{+2.9}_{-0.8}$	$1.9^{+0.4}_{-0.4}$	$0.12^{+0.05}_{-0.07}$	4.5/4
2010	—	$4^{+3}_{-1}$	$3.8^{+0.4}_{-0.5}$	$0.36^{+0.08}_{-0.1}$	12.4/25
2016	—	$3.1^{+2.1}_{-0.9}$	$32^{+5}_{-5}$	$2.6^{+0.5}_{-0.7}$	4.1/9
$N_{\text{H}}$ and $\Gamma/kT$ tied and joint fit of observations					
power law					
2004	$3^{+6}$	$1.7^{+0.4}_{-0.4}$	$0.4^{+0.3}_{-0.2}$	$0.2^{+0.1}_{-0.06}$	20.4/39
2010	—	—	$0.9^{+0.7}_{-0.3}$	$0.4^{+0.3}_{-0.1}$	—
2016	—	—	$7^{+5}_{-3}$	$3^{+2}_{-1}$	—
APEC					
2004	$2^{+5}$	$7^{+22}_{-3}$	$1.3^{+0.4}_{-0.3}$	$0.17^{+0.06}_{-0.04}$	20.6/39
2010	—	—	$3.0^{+0.9}_{-0.5}$	$0.4^{+0.1}_{-0.07}$	—
2016	—	—	$24^{+8}_{-5}$	$3^{+1}_{-0.6}$	—
$N_{\text{H}}$ frozen and $\Gamma/kT$ tied and joint fit of observations					
power law					
2004	$7.7^*$	$2.0^{+0.2}_{-0.2}$	$0.6^{+0.2}_{-0.1}$	$0.2^{+0.2}_{-0.1}$	21.1/40
2010	—	—	$1.4^{+0.3}_{-0.2}$	$0.35^{+0.06}_{-0.06}$	—
2016	—	—	$11^{+2}_{-2}$	$2.8^{+0.4}_{-0.3}$	—
APEC					
2004	$7.7^*$	$4^{+1}_{-0.8}$	$1.7^{+0.3}_{-0.3}$	$0.15^{+0.04}_{-0.07}$	21.9/40
2010	—	—	$3.9^{+0.3}_{-0.4}$	$0.35^{+0.06}_{-0.06}$	—
2016	—	—	$31^{+5}_{-4}$	$2.8^{+0.4}_{-0.4}$	—

lines, while in 2008 October and 2013 September–October, double-peaked  $\text{H}\alpha$  and  $\text{H}\beta$  were present.

We estimate the size of the circumstellar disc around MT91 213 using the relation from Hanuschik (1989), which connects circumstellar disc radius  $R_{\text{disc}}$  and stellar radius  $R_{\text{OB}}$  to the  $\text{H}\alpha$

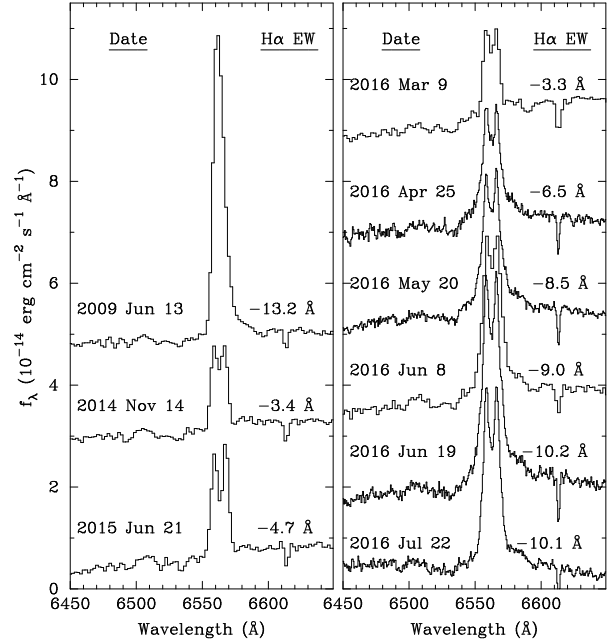


**Figure 7.**  $\text{H}\alpha$  region of spectra of MT91 213 (see Table 5). Spectra have been shifted vertically for clarity. 2009 spectrum is the same as appears in Camilo et al. (2009). Absolute flux densities for MDM spectra are not reliable due to the narrow ( $1''$ ) slit width used.

EW, i.e.

$$\log(R_{\text{disc}}/R_{\text{OB}}) = 0.4 + 0.64 \log(-\text{EW}). \quad (1)$$

Our EW measurements of MT91 213 indicate that its circumstellar disc has varied in size by more than a factor of two, from 5 to  $13R_{\text{OB}}$  (see Table 5). For typical B0 V stars,  $R_{\text{OB}} \sim 8R_{\odot}$  (Vacca et al. 1996), which yields a range of  $R_{\text{disc}}$  from  $\sim 40R_{\odot} = 3 \times 10^7 \text{ km} = 0.2 \text{ AU}$  to  $\sim 100R_{\odot} = 7 \times 10^7 \text{ km} = 0.5 \text{ AU}$ . Approximately similar values of  $R_{\text{disc}}$  are obtained using the separation of the double peaks seen in spectra from 2014 to 2016. However for these later spectra, EW varies by a factor of about three (implying disc size change of about two), while peak separation does not change significantly. It is also noteworthy that broad wings appear in the  $\text{H}\alpha$  spectra, beginning in 2016 Apr 25, when EW increases (see Fig. 8, which shows X-ray and optical light curves since late 2014). These broad wings could be due to higher wind velocities, which could cause the observed increase in X-ray emission.

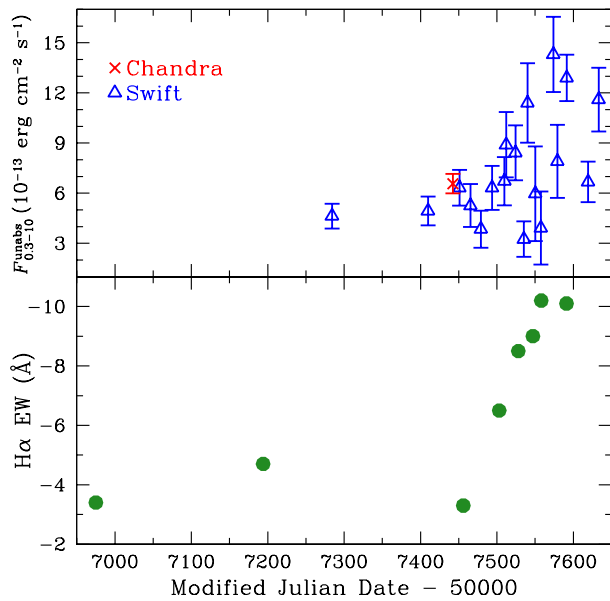
## 5 DISCUSSION

In this work, we described recent multiwavelength observations of the high-energy binary system containing the 143 ms radio pulsar PSR J2032+4127 and the B0 Ve companion star MT91 213. The orbit is very eccentric ( $0.94 < \epsilon < 0.99$ ) and large ( $P_{\text{orb}} \approx 45 - 50 \text{ yr}$ ), and the pulsar is accelerating rapidly towards periastron passage in 2017 November. We updated orbital parameters of the system obtained via radio monitoring, combined with *Fermi* LAT observations, of the pulsar. Archival and recent *Chandra* and *Swift* observations show that the PSR J2032+4127/MT91 213 system has brightened significantly in X-rays, especially within the last year as it approaches periastron.

We can understand the current and past behavior of the

**Table 5.** Optical spectra of MT91 213.

Date	Telescope	Instrument	Resolution Å	H $\alpha$ EW Å	$R_{\text{disc}}/R_{\text{OB}}$
2009 Jun 13	MDM 2.4 m	Modspec	3.5	-13.2	13.1
2014 Nov 14	MDM 2.4 m	Modspec	3.5	-3.4	5.5
2015 Jun 21	MDM 2.4 m	Modspec	3.5	-4.7	6.8
2016 Mar 9	MDM 1.3 m	Modspec	3.5	-3.3	5.4
2016 Apr 25	Liverpool 2 m	FRODOSpec	1.2	-6.5	8.3
2016 May 20	Liverpool 2 m	FRODOSpec	1.2	-8.5	9.9
2016 Jun 8	MDM 2.4 m	Modspec	3.5	-9.0	10
2016 Jun 19	Liverpool 2 m	FRODOSpec	1.2	-10.2	11
2016 Jul 22	Liverpool 2 m	FRODOSpec	1.2	-10.1	11

**Figure 8.** X-ray and optical light curves of PSR J2032+4127/MT91 213 from late 2014 to 2016. Top: Points (and  $1\sigma$  error bars) are *Chandra* (crosses) and *Swift* (triangles) unabsorbed 0.3–10 keV flux (see Table 2). Bottom: Circles are H $\alpha$  EW measurements (see Table 5).

PSR J2032+4127/MT91 213 system by comparing it to the high-energy binary pulsar system PSR B1259–63/LS 2883, since the two systems have many similarities. PSR B1259–63 is a 47.76 ms radio pulsar in an eccentric ( $\epsilon \approx 0.87$ ) 3.4 yr orbit with LS 2883, which is a 09.5 Ve star (Johnston et al. 1992; Negueruela et al. 2011). PSR B1259–63/LS 2883 has been observed across the electromagnetic spectrum during each periastron passage since its discovery (see, e.g. Chernyakova et al. 2015, for discussion of the most recent passage in 2014), as well as around apastron (see, e.g. Hirayama et al. 1999). The resulting studies show that its multi-wavelength emission can be understood as shock interaction between the relativistic wind emitted by the pulsar and the circumstellar disc and wind of the companion star (Tavani & Arons 1997). However, in attempting to extrapolate the observed behavior of PSR B1259–63 to that of PSR J2032+4127, it is important to note that the binary separation at apastron is  $\sim 11$  AU in the case of PSR B1259–63, while PSR J2032+4127 has only been observed up to this point at a binary separation  $> 10$  AU. At this large distance, the wind from MT91 213 is possibly tenuous, and its collision with

the pulsar wind is possibly weak. Also LS 2883 is four times more luminous and a different stellar type (Negueruela et al. 2011), so its wind properties are likely different from that of MT91 213.

For *Chandra* observations taken in 2002, 2004, and around 2010, PSR J2032+4127 was quite distant from MT91 213, at a binary separation of  $\geq 30$  AU (see Fig. 1). Thus the observed X-ray emission [with  $L_X \approx (0.05 - 0.2) \times 10^{32}$  erg  $s^{-1} (d/1.3 \text{ kpc})^2$ ] could be due to what is effectively an isolated Be star or an isolated young pulsar. In the former case, bright X-ray emission from powerful wind shocks of O stars is quite common, and spectra are often fit with an optically thin thermal plasma model (as performed in Section 3.1); the source of X-ray emission from stars of later stellar types is less certain, with a transition around early B stars, like MT91 213, that have  $L_X \sim 10^{30} - 10^{32}$  erg  $s^{-1}$  (Berghöfer et al. 1997; Gagné et al. 2011; Nazé et al. 2014). Using the relation between X-ray and bolometric luminosities,  $\log L_X/L_{\text{bol}} \approx -7.2$ , found for O and bright B stars (although there is large dispersion at the luminosity of stars similar to MT91 213; Rauw et al. 2015), we find  $L_X = 4 \times 10^{30}$  erg  $s^{-1}$ , which matches the X-ray luminosity of MT91 213 in 2002.

For isolated pulsars, X-ray radiation can have non-thermal and thermal contributions. Non-thermal emission can be generated by a relativistic wind, which produces a ratio between X-ray luminosity to rotational energy loss of  $L_X/\dot{E} \lesssim 10^{-3}$  and a spectrum that is best-fit by a power-law with  $\Gamma \approx 1 - 3$  (Becker 2009). For PSR J2032+4127,  $\dot{E} = 1.5 \times 10^{35}$  erg  $s^{-1}$ , and the measured power law is  $\Gamma \approx 1.5 - 2.5$  (Table 4). Thus a pulsar wind can easily be the source of observed X-rays. Meanwhile, thermal emission for intermediate age ( $\sim 10^5$  yr) neutron stars gives  $L_X \sim 10^{31} - 10^{33}$  erg  $s^{-1}$  (see, e.g. Potekhin et al. 2015).

The more recent observations since late 2015 show significant brightening in X-rays (see Fig. 6), with  $L_X \approx (0.6 - 2.9) \times 10^{32}$  erg  $s^{-1} (d/1.3 \text{ kpc})^2$ . Although these luminosities are somewhat lower than the X-ray luminosity seen for PSR B1259–63 at apastron ( $L_X \approx 5 \times 10^{32}$  erg  $s^{-1}$ ; Hirayama et al. 1999; Uchiyama et al. 2009), the brightening of PSR J2032+4127 suggests that the pulsar has entered the regime where the pulsar wind is interacting strongly with the Be star wind. X-ray spectral studies of PSR B1259–63 find that most observations made by *Chandra*, *Suzaku*, *Swift*, and *XMM-Newton* can be fit with a power law model (see, e.g. Tavani & Arons 1997; Chernyakova et al. 2009, 2014). Chernyakova et al. (2006, 2009) and Uchiyama et al. (2009) show that the value of  $\Gamma$  varies with orbital phase and that  $\Gamma$  changes from 1.8 around apastron to 1.2 right before the pulsar enters the circumstellar disc of LS 2883 at periastron, a decline that is similar to what is found from our limited spectra of PSR J2032+4127 (see Table 4).

The PSR J2032+4127/MT91 213 system will continue to be monitored across the electromagnetic spectrum as the pulsar approaches periastron. When it is near periastron, the system may brighten even more if the pulsar accretes from the circumstellar disc of the Be star. PSR J2032+4127/MT91 213 will thus serve as an invaluable tool for comparing and contrasting to the very well-studied and previously unique gamma-ray binary PSR B1259–63/LS 2883.

## ACKNOWLEDGEMENTS

The authors are indebted to Paul Ray for his support and careful reading of the manuscript. The authors thank Maria Chernyakova for helpful comments and Belinda Wilkes and the *Chandra* team for conducting the 2016 DDT observation. WCGH acknowledges support from the United Kingdom Science and Technology Facilities Council (UK STFC). Pulsar research at Jodrell Bank Centre for Astrophysics is supported by a Consolidated Grant from UK STFC. The *Fermi* LAT Collaboration acknowledges generous ongoing support from a number of agencies and institutes that supported both development and operation of the LAT as well as scientific data analysis. These include the National Aeronautics and Space Administration and Department of Energy in the United States, Commissariat à l’Energie Atomique and Centre National de la Recherche Scientifique/Institut National de Physique Nucléaire et de Physique des Particules in France, Agenzia Spaziale Italiana and Istituto Nazionale di Fisica Nucleare in Italy, Ministry of Education, Culture, Sports, Science and Technology (MEXT), High Energy Accelerator Research Organization (KEK), and Japan Aerospace Exploration Agency (JAXA) in Japan, and K. A. Wallenberg Foundation, Swedish Research Council, and Swedish National Space Board in Sweden. Additional support for science analysis during the operations phase is gratefully acknowledged from the Istituto Nazionale di Astrofisica in Italy and Centre National d’Études Spatiales in France. The Liverpool Telescope is operated on the island of La Palma by Liverpool John Moores University in the Spanish Observatorio del Roque de los Muchachos of the Instituto de Astrofisica de Canarias with financial support from UK STFC.

## REFERENCES

Abdo A. A., et al., 2009, *Science*, 325, 840  
 Abdo A. A., et al., 2013, *ApJS*, 208, 17  
 Acero F., et al., 2015, *ApJS*, 218, 23  
 Acero F., et al., 2016, *ApJS*, 223, 26  
 Becker W., 2009, in Becker W., ed., *Ap&SSL 357, Neutron Stars and Pulsars*. Springer-Verlag, Berlin, p. 91  
 Berghöfer T. W., Schmitt J. H. M. M., Danner R., Cassinelli J. P., 1997, *A&A*, 322, 167  
 Burrows D. N., et al., 2005, *Sp. Sci. Rev.*, 120, 165  
 Camilo F., et al., 2009, *ApJ*, 705, 1  
 Chernyakova M., Neronov A., Lutovinov, A., Rodriguez, J., Johnston, S., 2006, *MNRAS*, 367, 1201  
 Chernyakova M., Neronov A., Aharonian F., Uchiyama Y., Takahashi T., 2009, *MNRAS*, 397, 2123  
 Chernyakova M., et al., 2014, *MNRAS*, 439, 432  
 Chernyakova M., et al., 2015, *MNRAS*, 454, 1358  
 Dubus G., 2013, *A&A Rev.*, 21, 64  
 Gagné M., et al., 2011, *ApJS*, 194, 5  
 Gehrels N., 1986, *ApJ*, 303, 336  
 Hanuschik R. W., 1989, *Ap&SS*, 161, 61

Hirayama M., Cominsky L. R., Kaspi V. M., Nagase F., Tavani M., Kawai N., Grove J. E., 1999, *ApJ*, 521, 718  
 Hobbs G. B., Edwards R. T., Manchester R. N. 2006, *MNRAS*, 369, 655  
 Hohle M. M., Neuhäuser R., Schutz B. F., 2010, *Astron. Nachr.*, 331, 349  
 Johnston S., Manchester R. N., Lyne A. G., Bailes M., Kaspi V. M., Qiao G., D’Amico N., 1992, *ApJ*, 387, L37  
 Kerr M., 2011, *ApJ*, 732, 38  
 Kiminki D. C., et al., 2007, *ApJ*, 664, 1102  
 Kiminki D. C., Kobulnicky H. A., Vargas Álvarez C. A., Alexander M. J., Lundquist M. J., 2015, *ApJ*, 811, 85  
 Klus H., Ho W. C. G., Coe M. J., Corbet R. H. D., Townsend L. J., 2014, *MNRAS*, 437, 3863  
 Lyne A. G., Stappers B. W., Keith M. J., Ray P. S., Kerr M., Camilo F., Johnson T. J., 2015, *MNRAS*, 451, 581  
 Massey P., Thompson A. B., 1991, *AJ*, 101, 1408  
 Murakami H., Kitamoto S., Kawachi A., Nakamori T., 2011, *PASJ*, 63, S873  
 Nazé Y., Petit V., Rinbrand M., Cohen D., Owocki S., Ud-Doula A., Wade G. A., 2014, *ApJS*, 215, 10  
 Negueruela I., Ribó M., Herrero A., Lorenzo J., Khangulyan D., Aharonian, F. A., 2011, *ApJ*, 732, L11  
 Page D., Geppert U., Weber F., 2006, *Nucl. Phys. A*, 777, 497  
 Potekhin A. Y., Pons J. A., Page D., 2015, *Space Sci. Rev.*, 191, 239  
 Rauw G., et al., 2015, *ApJS*, 221, 1  
 Ray P. S., et al., 2011, *ApJS*, 194, 17  
 Reig P., 2011, *Ap&SS*, 332, 1  
 Reig P., Nersesian A., Zezas A., Gkouvelis L., Coe M. J., 2016, *A&A*, 590, 122  
 Salas J., Maiz Apellaniz J., Gamen R. C., Barba R. H., Sota A., Sanchez-Bermudez J., Alfaro E. J., 2013, *ATel* 5571  
 Tavani M., Arons J., 1997, *ApJ*, 477, 439  
 Uchiyama Y., Tanaka T., Takahashi T., Mori K., Nakazawa K., 2009, *ApJ*, 698, 911  
 Vacca W. D., Garmany C. D., Shull J. M., 1996, *ApJ*, 460, 914  
 Walborn N. R., 1973, *ApJ*, 180, L35  
 Wilms J., Allen A., McCray R., 2000, *ApJ*, 542, 914  
 Wright N. J., Drew J. E., Mohr-Smith M., 2015, *MNRAS*, 449, 741  
 Yakovlev D. G., Pethick C. J. 2004, *ARA&A*, 42, 169